Computers and Electronics in Agriculture 151 (2018) 276–285

Contents lists available at ScienceDirect

Computers and Electronics in Agriculture

journal homepage: www.elsevier.com/locate/compag

Acoustic tomography based on hybrid wave propagation model for tree decay detection

Lei Liu, Guanghui Li*

School of Internet of Things (IoT) Engineering, Jiangnan University, 214122 Wuxi, China
Engineering Research Center of IoT Technology Applications (Ministry of Education), Jiangnan University, 214122 Wuxi, China

ARTICLE INFO

Keywords:
Acoustic tomography
Curved-ray inversion
Hybrid wave propagation model
Internal defect
Urban trees

ABSTRACT

Acoustic wave technologies have been used in wood defect detection for many years. Various tomographic imaging algorithms have been proposed to construct two dimensional acoustic velocity maps that serve as the scientific evidence of tree's internal condition. Many previously proposed algorithms were based on the assumption that acoustic waves propagate along straight rays in the cross sections of trees. To simulate the acoustic wave propagation more realistically, this paper proposed a tomographic imaging method based on a hybrid wave propagation model (HWPM) that includes two velocity inversion phases: straight-ray inversion and curved-ray inversion. The straight-ray inversion was first applied to obtain the preliminary velocity distribution, followed by the curved-ray inversion to refine the velocity distribution. A velocity correction factor was determined for each grid cell following each inversion iteration, and then was used to derive a new velocity value for each corresponding cell. The maximum and minimum velocity constraints were imposed on the newly-computed velocities, and some velocity constraints of grid cells were also imposed to address the nonuniqueness problem commonly existed in velocity inversion and generate a more accurate tomographic image. To evaluate the effectiveness of the hybrid inversion method, we conducted multipath acoustic wave testing on three short log sections (one sound and two with artificial defect) in the laboratory and four live trees in Yangzhou Slender West Lake Park, Jiangsu Province, China. Time-of-flight data was collected by PiCUS Tomograph tool and used to generate tomographic images with both Simultaneous iterative reconstruction technique (SIRT) and the proposed hybrid inversion method to make a comparison. Micro-drilling tests were conducted on the live trees to determine the internal condition and served as the basis for evaluating the tomographic images. Our results indicate that the hybrid wave propagation model is effective in constructing acoustic tomographic images that are reasonably accurate in detecting the internal defects of urban trees.

1. Introduction

Urban trees play a significant role in our daily life and are valuable assets to communities and a healthy environment. Defects, both external and internal, can develop throughout the life cycle of a tree. Detecting the internal structural defects that are hidden from view on tree trunks is a big challenge to arborists and tree managers. Both public safety and urban forest conservation concerns support strong interest in developing and applying more rapid and precise diagnostic tools to detect decay and other types of structural defects in trees (Allison et al., 2006).

Acoustic wave method has proved to be an appropriate technique for assessing internal conditions of wood and locating moderate to severe internal decay in trees (Lin et al., 2013; Gao et al., 2014; Merlo et al., 2014). Comparing to other nondestructive methods such as X-ray, computer tomography (CT), and ground-penetrating radar, acoustic wave techniques are regarded as low-cost, user friendly, and suitable to many field applications (Brancheriau et al., 2012; Wang, 2013). Several commercial acoustic tomography tools (such as ArborSonic 3D Acoustic Tomograph, PiCUS Sonic Tomograph, and ARBOTOM®) have been developed and are currently being used to perform multi-path acoustic measurements on urban trees and obtain two dimensional tomographic images of tree's cross sections. Kana et al. (2015) measured a green disk of Zelkova serrata with different sizes of artificial circular cavities and reconstructed contour map by acoustic tomography. Gregory et al. (2016) developed a protocol to use the PiCUS 3 under difficult conditions and especially for tropical tree species with highly irregular trunk outlines that can cause aberrant tomograms. Espinosa et al. (2017) presented a segmentation methodology to identify defective regions in cross-section tomographic images obtained with an Arbotom device.

* Corresponding author at: School of Internet of Things (IoT) Engineering, Jiangnan University, Wuxi, China.
E-mail address: ghli@jiangnan.edu.cn (G. Li).

https://doi.org/10.1016/j.compag.2018.06.020
Received 6 April 2018; Received in revised form 4 June 2018; Accepted 9 June 2018
Available online 15 June 2018
0168-1699/

Different inversion algorithms based on straight-ray propagation have been used in acoustic tomography. The cell-based back-projection algorithm split the polygon of sensors into cells and the slowness (reciprocal of velocity) of each cell was assumed constant (Divos and Divos, 2005). By using the elementary back-projection approximation, the slowness of each grid cell equals to the average of the line slowness values of lines intersecting the cell and the resolution is determined by the number of cells. Filtered back-projections can be used to perform an inverse transformation to obtain the slowness function from the time-of-flight (TOF) data by assuming the stress waves propagate in straight lines (Brancheriau et al., 2012). Feng et al. (2014) put forward an image reconstruction method that utilized an interpolation algorithm which estimated the velocity value of the unknown grid cells based on the site information of the known cells. Du et al. (2015) proposed an improved ellipse-based spatial interpolation method which could be used to estimate the velocity value of a grid cell by the elliptic affected zones corresponding to the nearby velocity rays and a velocity compensation method was applied to obtain more accurate input data for spatial interpolation because of the anisotropic property of trees.

Li et al. (2014) investigated the stress wave velocity patterns in cross sections of black cherry trees and developed an analytical model of stress wave velocity in healthy trees. Their theoretical analysis indicated that the ratio of tangential velocity to radial velocity approximated a parabolic curve with symmetric axis $h = 0$ (h is the angle between tangential direction and radial direction). The experimental results of the sound cross sections showed that the measured velocity patterns were in good agreement with the theoretical analysis. The tomograms of the cross sections with internal decay reflected the anomaly of velocity pattern and the proposed theoretical velocity model can be used as a diagnostic tool to detect internal decay of live trees.

However, with the existence of cavity or other structural defects, the propagation path of acoustic waves may be altered, that is, the waves may not propagate along a straight ray and the transmitting ray from the source sensor may be curved by bypassing the defect to reach the receiver sensor. A wave propagating model based on curved rays can more closely reflect the true condition of a tree, thus allowing a better simulation of acoustic wave transmission.

Acoustic wave may propagate along curved path through a heterogeneous medium, and the curved-ray propagation model has been employed in many fields. The U.S. Bureau of Mines' (USBM) second generation tomographic program, BOMCRATR, performs curved-ray calculations using the shooting method which find the path to a particular receiver by tracing rays with different takeoff angles from the source and interpolating until one passes sufficiently close to the receiver (Tweeton, 1992). The third-generation USBM tomographic program, MIGRATOM, uses a modeling migration of a continuous wavefront to address various mining-related problems by reconstructing the velocity distribution in the rock mass. MIGRATOM has been proved effective with both synthetic and field data sets (Jackson and Tweeton, 1994).

In tomographic imaging, the mathematical nonuniqueness of the solutions is a critical problem that affects the reconstruction (Jackson, 1979; Jackson and Tweeton, 1994). The insufficient measured data or limited range of viewing angles results in singular matrices in the velocity inversion, because the travel-time equations are not all linearly independent and thus many solutions can be found to fit the data equally well. Simultaneous iterative reconstruction technique (SIRT) algorithm is a traditional image reconstruction method which can solve the sparse matrix problem. There are also some strategies for reducing the nonuniqueness. For example, constraints may be imposed on the solution and be incorporated into the inversion to limit the range of the possible solutions (Jackson and Tweeton, 1994; Socco et al., 2004).

To improve the accuracy and reliability of tomographic technique, we proposed an imaging method based on a hybrid wave propagation model (HWPM) to reconstruct acoustic tomographic images using the measured TOF data. The hybrid wave propagation model applied both straight-ray and curved-ray transmission models for iterative image reconstruction. The effectiveness of the hybrid inversion method was examined through actual multipath acoustic wave testing conducted on log samples and live trees.

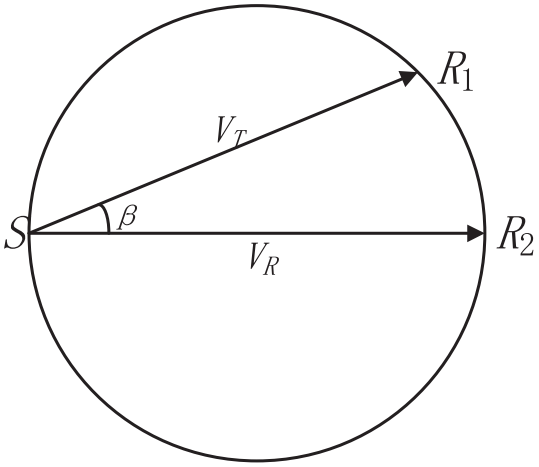

Fig. 1. Stress wave propagation in the cross-section of tree trunk.

2. Principle of tomographic imaging of live trees

2.1. Wave velocity pattern in sound healthy trees

A better understanding of wave velocity patterns in trees is important to develop reliable and effective imaging software for internal decay detection. For simplicity, we assume that the cross section of tree trunk is an ideal circularity (Fig. 1). In Fig. 1, S represents the source sensor, and R_1 and R_2 represents the receiver sensors. Stress waves propagate from the source sensor to the receiver sensors. SR_1 is the tangential direction, and SR_2 is the radial direction. V_T is the tangential wave velocity, V_R is the radial wave velocity, and β is the angle between radial direction and tangential direction. Generally, the stress wave velocity along radial direction is the largest and the velocity will decrease with the increment of the direction angle β. Li et al. (2014) presented an analytical model of the ratio of tangential velocity to radial velocity in sound trees, which approximates a second-order parabolic curve with respect to the symmetric axis $\beta = 0$ as following equation (1). Fig. 2 shows the wave velocity pattern of one sample tree. Here, the angle β was converted into radian unit ($1^\circ = \pi/180$). The relationship between velocity ratio V_T/V_R and angle β was statistically in a parabolic curve, with a coefficient of determination $R^2 = 0.9989$. The coefficients of the second order polynomial regression are $a = -0.2062$, $b = -0.0096$, and $c = 1.0067$. It was noted that the coefficient of the first order term was close to zero and the constant

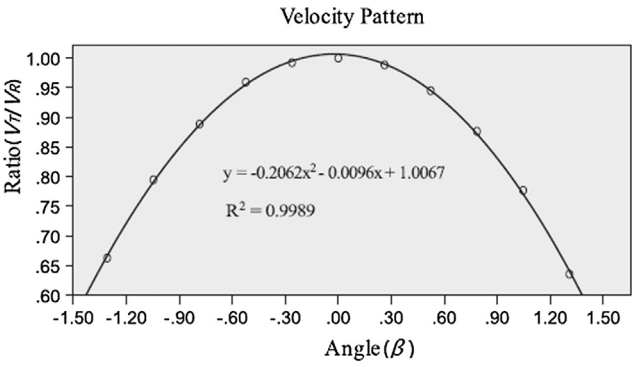

Fig. 2. Wave velocity pattern of sample trees.

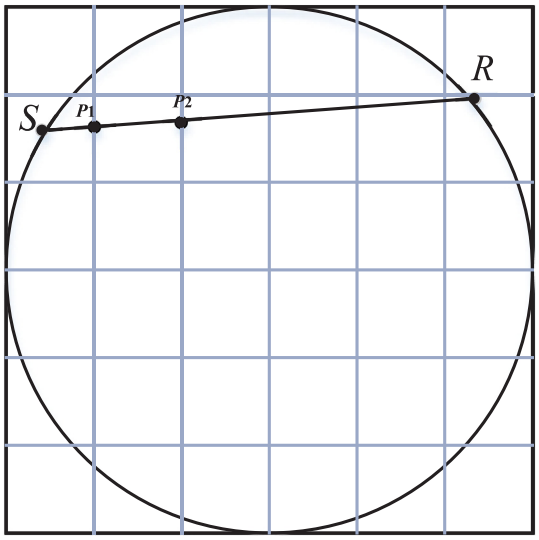

Fig. 3. The square grid cells of a cross-section of tree trunk.

close to 1, which is in good agreement with Eq. (1).

$$V_T/V_R \approx 1 - 0.2\beta^2 \tag{1}$$

Usually, the peripheral reference velocity V_0 is determined by calculating the average of the line velocities of the neighboring sensors. This velocity can be used as reference, because the sapwood of the tree is usually intact (Divos and Divos, 2005). Then, the reference velocity of each path can be computed from Eq. (1).

2.2. The principle of straight-ray velocity inversion and SIRT algorithm

Acoustic tomographic inversion is the process to derive the velocity distribution in the investigated cross section using the TOF data and the positions of sensors as inputs. Usually, the cross-section plane was divided into grid cells of suitable size as shown in Fig. 3. For instance, Fig. 3 shows a wave propagation path from the source S to the receiver R, and the wave travel time can be calculated by a line integral of the wave slowness along this path.

$$t = \int_S^R pdl \tag{2}$$

Here, p is the slowness of wave, and dl is the infinite small distance along the wave path. To reconstruct the velocity distribution, the domain is often divided into M grid cells, and the continuous function $p(x,y)$ is approximated by the discrete slowness distribution in each grid cell. Given the assumption that the slowness p is uniform in each cell, the integral (2) becomes a summation:

$$t_i = \sum_{j=1}^{M} p_{jd_{ij}} (i = 1, 2, ..., N) \tag{3}$$

where t_i is the travel time of the i^{th} wave path, p_j is the slowness of the j^{th} cell, d_{ij} is the segment intercepted by the i^{th} wave path on the j^{th} cell and N is the number of the propagation paths. Then the summation can be expressed in matrix form as follows:

$$T = DP \tag{4}$$

where T and P are the time and slowness vectors respectively, and D represents the intercepted segments matrix.

Tomographic imaging involves solving for P, the slowness vector, given the travel-time matrix T. This requires that the matrix of path lengths D be calculated. SIRT uses an approximate solution known as back-projection to compute vector P which uses a row-normalized transpose.

$$P = (D^*)^T T \tag{5}$$

Here, the matrix D^* is obtained by dividing each row of D, which corresponds to a particular path, by the square of the path length. Thus, the slowness of each grid cell can be calculated as follows:

$$P_j = \sum_{i=1}^{N} \frac{D_{ij} T_i}{D_i^2} (j = 1, 2, ...,M) \tag{6}$$

where P_j is the slowness in the j^{th} grid cell, N is the number of propagation paths, D_{ij} is the segment intercepted by the i^{th} wave path in the j^{th} grid cell, T_i is the travel time of the i^{th} wave path, D_i is the distance of the i^{th} wave path and M is the number of the grid cells.

2.3. Curved-ray velocity inversion

Due to the existence of cavity or other defective areas, the wave may not propagate along the straight path. In other words, the propagation path may take the bypass of the defective area and propagate along a curved path from the source to the receiver. We employ the Huygens principle to better simulate the propagation of the wave.

Initially applied in optics, Huygens principle is capable of simulating the propagation of a wavefront through a heterogeneous material by regarding each point on the wavefront as a consequent point source of wave (Saito, 1989). The Huygens principle is described as follows.

In Fig. 4, at t_1 time, an initially circular wavefront consisting of several points (i.e. P_1, P_2, and P_3 in Fig. 4) is generated from the source position with different takeoff angles. By constructing the circular wavelets about a number of points on the current wavefront, new points are constructed which will constitute the next wavefront. The radius of each wavelet is proportional to the local velocity of the point (e.g. v_1 is the velocity of P_1). The locus of constructive interference is approximated by lines tangent to adjacent Huygens wavelets. Each point on the current wavefront is advanced for the next time step (i.e. dt) to a position on its wavelet midway between tangent points as $P_1(t_1 + dt)$, $P_2(t_1 + dt)$, and $P_3(t_1 + dt)$ in Fig. 4. Thereafter the consequent wavefronts are constructed in a series of time steps. With the expansion of the wavefront, new points are added by interpolation, and those points are deleted when they have travelled a certain distance outside the region of interest.

3. Tomographic image reconstruction based on hybrid wave propagation model

We proposed a tomographic imaging method based on hybrid wave propagation model (HWPM). HWPM applied both straight-ray and

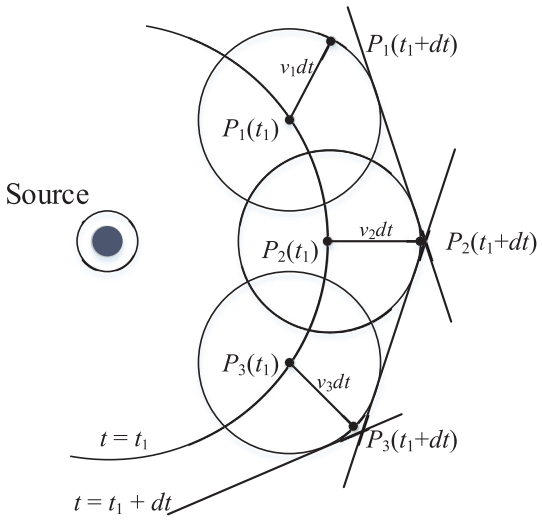

Fig. 4. Schematic illustration of Huygens principle.

curved-ray wave propagation model for iterative image reconstruction. During the iterative inversion process, some constraints were imposed on the grid cells to address the nonuniqueness problem of solution. The velocity inversion based on imaging procedure of HWPM is described as follows.

Step 1, Construction of initial velocity distribution of cross section of tree trunk. To inverse the velocity distribution iteratively, an initial velocity value is assigned to each grid cell at the beginning. Here, we assumed that the initial velocity of each cell is identical. This initial velocity was a random value ranged from 1 to 3000 m/s. Eq. (1) can be employed to generate the reference velocity of each propagation ray in the cross section. There may exist several paths in one grid cell, the average value of the velocities of these paths was taken as the reference velocity of the grid cell.

Step 2, Velocity inversion based on straight-ray wave propagation model. In one straight-ray iteration, the acoustic wave propagates along the straight paths between each pair of sensors. Eq. (6) can be utilized to compute the velocity correction factors of each grid cell which will be later assigned to the corresponding grid cell to generate the new velocity value. After the new velocity value of each grid cell was calculated, some constraints will be imposed on the newly-computed velocity value. Here, the maximum and minimum velocity constraints were adopted. By calculating the straight-ray distances between each pair of sensors and using the TOF data from PiCUS, the velocity of each straight propagation path will be obtained. The maximum velocity value of all the straight propagation paths will serve as the maximum velocity constraint, and the minimum velocity value of all the straight propagation paths will serve as the minimum velocity constraint. The newly-computed velocity value of each grid cell will be compared with these two velocity constraints. If the newly-computed velocity value was larger than the maximum velocity constraint, the maximum velocity constraint will replace the newly-computed velocity as the new velocity of the corresponding grid cell. If the newly-computed velocity value was less than the minimum velocity constraint, the minimum velocity constraint will replace the newly-computed velocity as the new velocity of the corresponding grid cell. After each straight-ray iteration, the propagation time between each pair of sensors will be calculated using Eq. (3) and then compared with the TOF data between each pair of sensors. The root mean square error of the time residuals (RMSE) will be calculated and compared with a given threshold ε_1. The iteration will not stop until RMSE was less than ε_1.

Step 3, Velocity inversion based on curved-ray propagation model. The curved-ray propagation contain two phases in each iteration. The first pass calculates the travel time of the rays and identifies the angles of the rays travelling from the source sensor to the receiver sensor, and the second pass traces the first pass and tabulates the segment distance intercepted by the grid cell. After two phases, Eq. (6) is employed to compute the velocity correction factors and the maximum and minimum velocity constraints are applied again. To reduce the complexity of the imaging algorithm, the number of iteration should not be too big. Our experiments showed that the curved-ray inversion often converged to a satisfactory result after about 3 iterations. As an example, the experimental result of one sample tree during curved-ray inversion was illustrated in Fig. 5, and RMSE tended to be stable after about 3 iterations.

Step 4, Reconstruction of tomographic image. After the velocity inversion iterations, the final velocity value (V_{cal}) of each grid cell can be calculated, along with the reference velocity value (V_{ref}) of each grid cell, the ratio of V_{cal}/V_{ref} can be calculated. The ratio will be compared with a given threshold ε_2, and if the ratio was less than ε_2, the grid cell can be determined as defective. After some image processing steps, the tomographic image of cross section can be generated with a multi-color scheme.

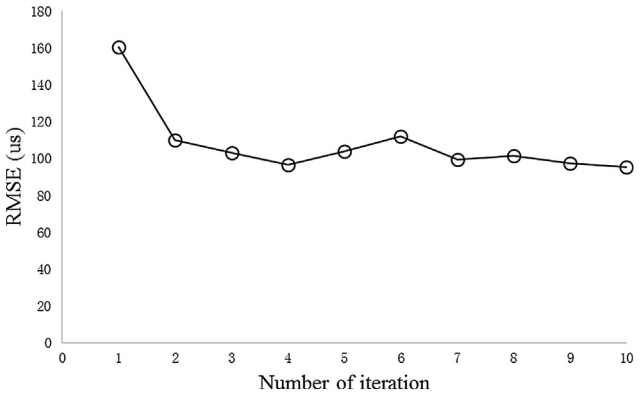

Fig. 5. The relationship between the computational precision and the number of iterations of HWPM.

4. Materials and methods

4.1. Acoustic data collection on log sections

Nondestructive testing experiments were conducted using logs and live trees as samples. The defective area of the logs in laboratory can be observed and evaluated visually, and it is convenient for comparing the tomographic image generated by HWPM with the actual situation. So the experiments with logs were carried out prior to those experiments on live trees. Three log samples including a sound cedar (*Cryptomeria fortunei*), a defective sapium (*Sapium sebiferum*) log with artificial cavity and a cedar log with artificial cavity were selected in laboratory tests. The log information was listed in Table 1. Here, column 6 presents the decay size of each sample, which denotes the diameter of the cavity.

The PiCUS Sonic Tomograph instrument (Argus Electronic, Rostock, Germany) was utilized to acquire the TOF data of the cross-section. Three logs were visually inspected first, and the photographic documentations of them were needed to later match tomograms to the physical log. According to the PiCUS manual, strategic placement of sensors was needed to match the trunk irregularities. After the sonic measurement with the PiCUS, the decay patterns can be visualized with both SIRT and HWPM.

4.2. Field testing on live trees

The field testing experiments of live trees were finished in Yangzhou Slender West Lake Park, Jiangsu Province, China. Tree selection procedures were conducted through application of the single-path stress wave test and visual examination mostly. The goal of the procedure was to obtain trees with different levels of internal decay. Four live trees with different defects including sabina (*Sabina chinensis*), cinnamon (*Cinnamomum camphora*), and willow (*Salix babylonica*) were selected as samples to evaluate the performance of HWPM.

Photographs from different positions around the tree were taken to later match tomograms to the physical tree. In field experiments, PiCUS instrument was used to collect the stress wave TOF data. Different from the laboratory experiments, the cross-section of live trees cannot be observed directly. So Resistograph® micro-drilling resistance instrument (Rinntech, Heidelberg, Germany) was used to evaluate the defective degree of live trees. The drilling resistance curve can reflect the internal condition along the drilling path precisely and verify the accuracy of the proposed imaging method. Four trees were first tested by the PiCUS instrument, and then the tomographic images were generated by SIRT and HWPM to make a comparison. Thereafter, trees were drilled by the Resistograph at the same height as stress wave testing to measure the defective degree of the cross-section along different paths.

The standing trees' information is shown in Table 2. As can be seen from Table 2, the measurement elevations above the ground are

Table 1
General information of log sections.

Tree species	Length (cm)	Diameter(cm)	Moisture content	Elevation (cm)	Decay size (cm)	Sensor deployment	Number of sensors
Cedar	30	27.6	12.5%	25	None (solid)	Round	10
Sapium	25	30	12.0%	20	9	Irregular	12
Cedar	45	30	12.0%	35	16	Irregular	12

different. The measurement plane was selected adjacent to the existence of the decay. Owing to the utilization of Resistograph® instrument, proximity to the roots may affect the results provided by that instrument.

5. Results and discussion

Both laboratory and field testing experiments were carried out to evaluate the performance of HWPM. To express the effects of the tomographic imaging of SIRT and HWPM visually, a 2D image with a multi-color scheme was used to represent the internal conditions of the samples. Light gray shows the sound area of the sample, the green, purple and blue areas are the defective areas with different defective degree of the trees.

5.1. Results of laboratory logs

For the laboratory experiments, three log samples were tested by PiCUS Sonic Tomograph instrument. Based on the TOF data collected by PiCUS, the tomographic images of SIRT were compared with those of HWPM.

The cedar sample is sound as shown in Fig. 6a. The tomographic comparison results are shown in Fig. 6b and c. Two methods have applied the wave velocity patterns in trees as a reference, and both the tomographic images were sound without any false decision from Fig. 6b and c.

The sapium sample is shown in Fig. 6d. There exists an artificial defect in the bottom area of the cross section. The comparison results of tomographic images are shown in Fig. 6e and f. The distances from the defective area to the corresponding sensors are marked in the figures. SIRT failed to detect the decay from Fig. 6e. In contrast, HWPM was capable of locating the defective area. However, some sound areas were detected incorrectly as defective areas from Fig. 6f and the distance to the 4th sensor was larger than the real condition. This may be caused by the inaccurate TOF data.

The cedar sample is shown in Fig. 6g. There exists an artificial defect in the right part of the cross section. The comparison results of tomographic images are shown in Fig. 6h and 6i. Two methods have successfully detected the decay in logs, but the decay size in the tomographic image of SIRT is smaller than the real condition. In contrast, the location and the size of the defective area generated by HWPM is in better agreement with the actual case.

For the laboratory logs, when processing the internal defects, such as the sapium sample and the defective cedar sample, tomography generated by SIRT tended to narrow the size of the defective area and the small decay in sapium sample was even ignored. However, HWPM adoped the curved-ray inversion which can simulate the propagation of acoustic wave around the defective area, and the size of the decay can be detected more precisely.

5.2. Results of live trees

Resistograph® micro-drilling instrument was used to evaluate the defective degree of live trees. In each resistance curve, the path *i-j* accords with the wave path in the tomographic image of the cross-section from the i^{th} sensor to the j^{th} sensor. Usually, some sharp decline can be found in the resistance curve, which indicates that there exist defects and consequently can help locate the defective area. To show the comparison intuitively, the boundaries of defective areas were marked with red lines for both tomographic images of SIRT and HWPM. Moreover, the white and black lines in the tomographic image represent the drilling paths with the Resistograph.

5.2.1. Sabina tree 1

Fig. 7a–c show the sabina tree 1 with a large cavity and the tomographic images generated by SIRT and HWPM, and Fig. 8a and b present the resistance curves of two paths. In Fig. 8a, part I represents the defective area in drilling path 1–7 and part II represents the sound area. Both methods were unable to detect the sound area showed by part (a) in Fig. 8a. Part I and III represent the sound areas in drilling path 4–10 and part II represents the defective area in Fig. 8b. Part (b) in Fig. 8b shows a sharp rise of resistance, which is caused by the knots within the cross section. The tomograms by SIRT and HWPM showed large shadows in the central areas of the cross-sections. Some severely damaged areas, as indicated by purple and blue, revealed significant heartwood decay in this tree.

5.2.2. Sabina tree 2

Fig. 7d–f show the sabina tree 2 with a large crack and the tomographic images generated by SIRT and HWPM, and Fig. 8c–e present the resistance curves of three paths. In Fig. 8c, part I and III represent the sound areas in drilling path 6–12 and part II represents the defective area. Part II represents the defective area in drilling path 7–12 and part I and III represent the sound areas in Fig. 8d. Part I and III represent the sound areas in drilling path 10–5 and part II represents the defective area in Fig. 8e. Tomograms with both methods contain large bands of acoustic shadows, which expand from the lateral sapwood to center. The tomograms revealed large lateral cracks of this tree which accords with the tree visually. The crack in the radial direction cut off the linear propagation of the acoustic waves and diverted them to a much longer travel path. From Fig. 8c, there exists a minor defect along path 6–12. SIRT failed to detect the decay and the tomographic image of HWPM

Table 2
General information of live trees.

Tree species	Circumference (cm)	Elevation(cm)	General description of trees
Sabina 1	138	100	There exist some bulges in sabina 1, and the deployment of sensors took the irregular form. Some branch deaths can be seen which may indicate the potential decay in this tree
Sabina 2	157	150	An obvious crack can be seen from this sabina tree, and irregular deployment of sensors was adopted
Cinnamon	150	150	Some evidences of insect activities can be observed in this tree. Due to the irregular trunk of this tree, sensors were deployed irregularly
Willow	120	50	Some small anomalies caused by fungal reproductive structures can be seen from this tree. A round and even deployment of sensors was used in this tree

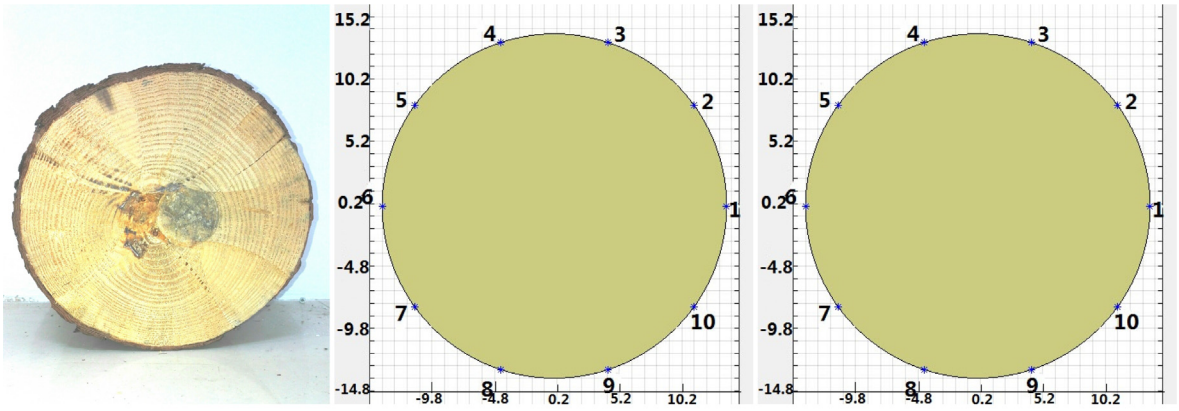

(a) Healthy cedar sample (b) Imaging result of SIRT (c) Imaging result of HWPM

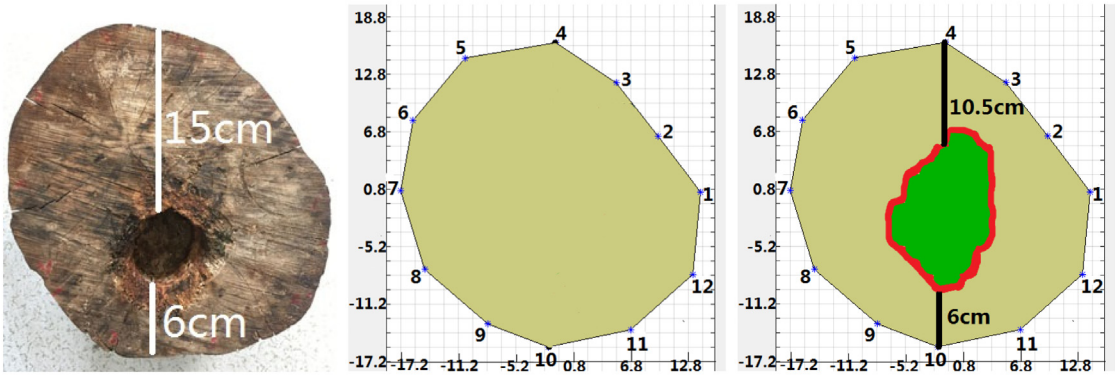

(d) Sapium sample (e) Imaging result of SIRT (f) Imaging result of HWPM

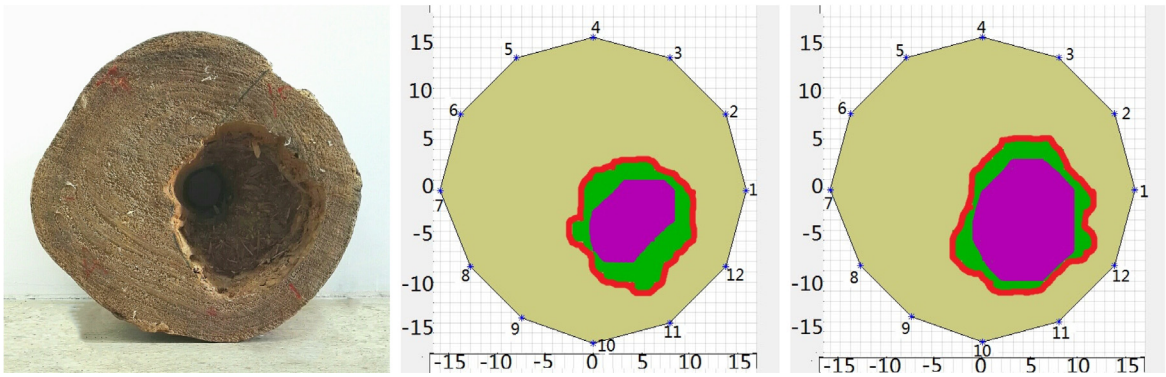

(g) Defective cedar sample (h) Imaging result of SIRT (i) Imaging result of HWPM

Fig. 6. The tomographic comparison results of sample logs.

was in good agreement with the resistance curve.

5.2.3. Cinnamon tree

Fig. 7g–i show the cinnamon tree and the tomographic images generated by SIRT and HWPM, and Fig. 8f–h present the resistance curves of three paths. In Fig. 8f, part I and III represent the sound areas in drilling path 1–7 and part II represents the defective area. Part II represents the defective area in drilling path 3–10 and part I and III represent the sound areas in Fig. 8g. In Fig. 8 h, part I and III represent the sound areas in drilling path 6–2 and part II represents the defective area. Tomogram of SIRT shows no acoustic shadow of path 1–7 in the cross-section. Comparatively, the minor defect such as small decay pocket or worm hole was detected by HWPM of path 1–7. Some severely damaged areas, as indicated by purple from Fig. 7i, reveal the small crack between the 1st sensor and the 2rd sensor which accords well with the visual inspection.

5.2.4. Willow tree

Fig. 7j–l show the willow tree and the tomographic images generated by SIRT and HWPM, and Fig. 8i and 8j present the resistance curves of two paths. In Fig. 8i, part I represents the defective area in drilling path 3–7 and part II represents the sound area. SIRT failed to detect the small defect along path 3–7. Part I represents the defective area in drilling path 5–9 and part II represents the sound area in Fig. 8j. The tomograms of SIRT and HWPM show the acoustic shadow near the perimeter of the cross-sections. The shape of the shadows with both

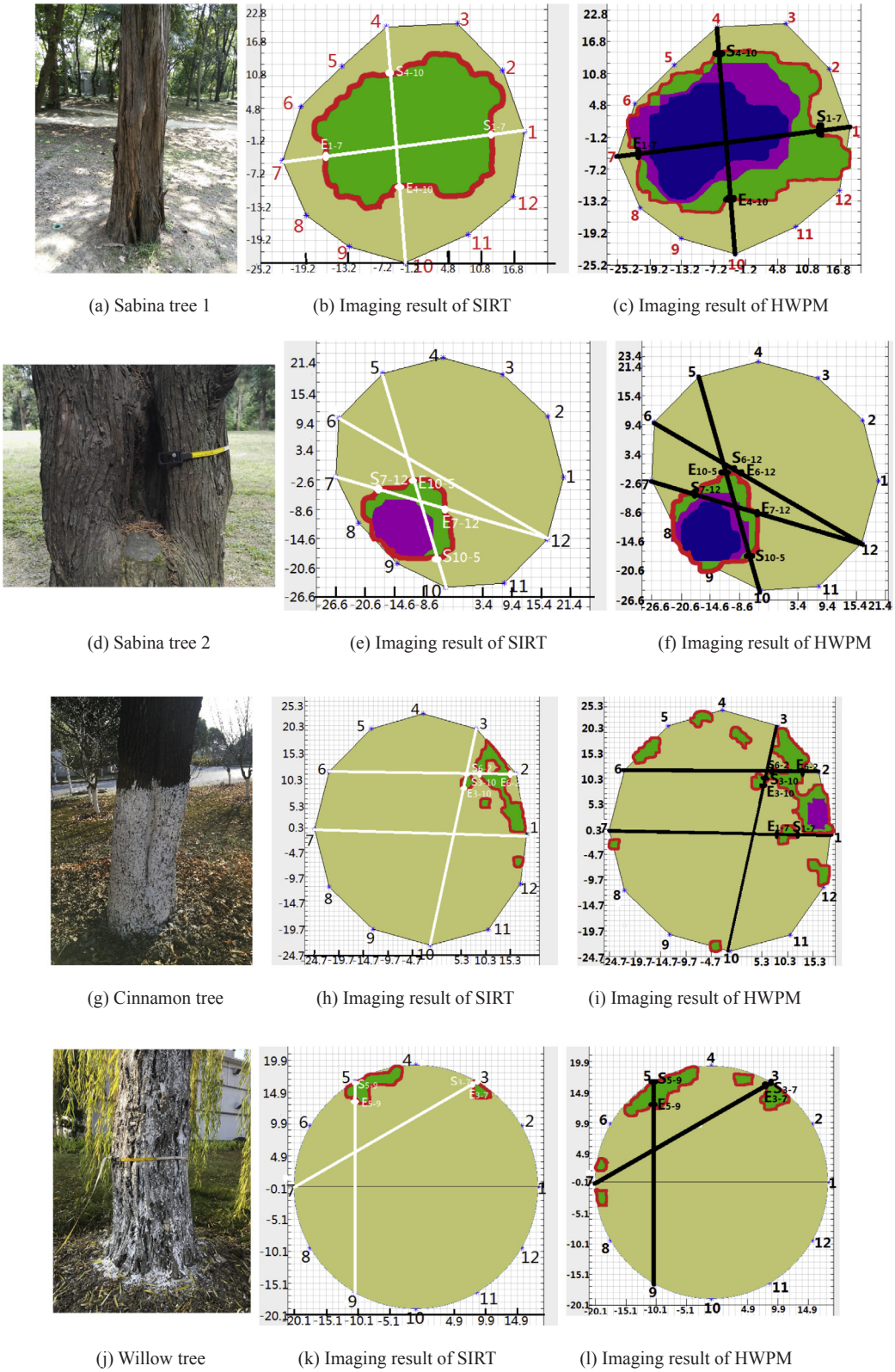

(a) Sabina tree 1 (b) Imaging result of SIRT (c) Imaging result of HWPM

(d) Sabina tree 2 (e) Imaging result of SIRT (f) Imaging result of HWPM

(g) Cinnamon tree (h) Imaging result of SIRT (i) Imaging result of HWPM

(j) Willow tree (k) Imaging result of SIRT (l) Imaging result of HWPM

Fig. 7. The tomographic comparison results of sample trees.

methods was approximate. The defective areas were indicated by green, which revealed the incipient decay there.

5.3. Sensitivity analysis of tomographic imaging in live trees

In both resistance curves and tomographic images of SIRT and HWPM, points $S_{i\text{-}j}$ and $E_{i\text{-}j}$ indicate the start point and end point of the defective area along drilling path *i-j*, respectively. To evaluate the effectiveness of HWPM quantitatively, we used *d* to denote the distances from $S_{i\text{-}j}$ or $E_{i\text{-}j}$ to the corresponding sensor along different drilling paths, which can reflect the location of the defective area on the cross-section.

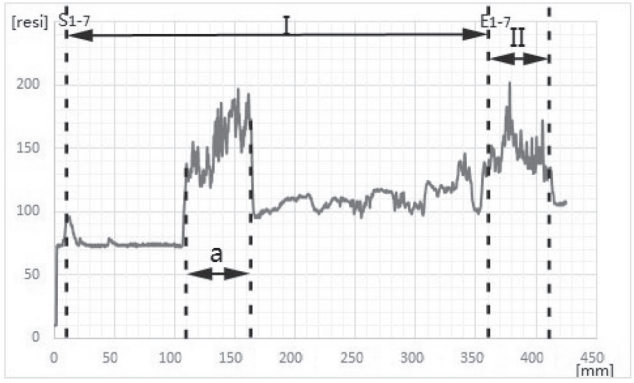

(a) Path 1-7

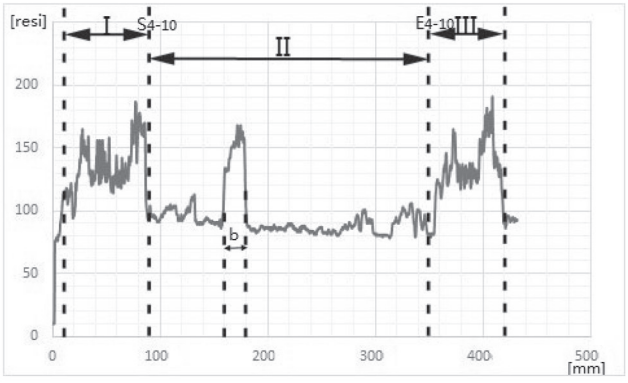

(b) Path 4-10

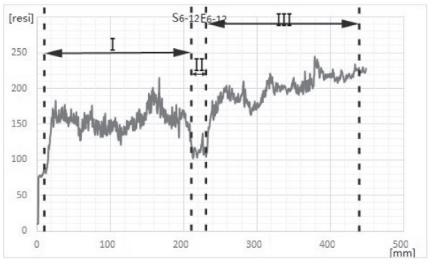

(c) Path 6-12

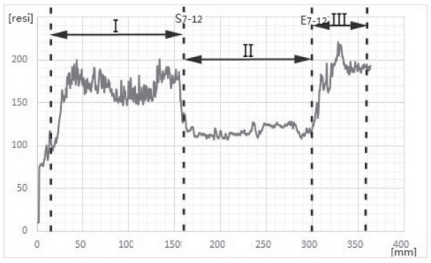

(d) Path 7-12

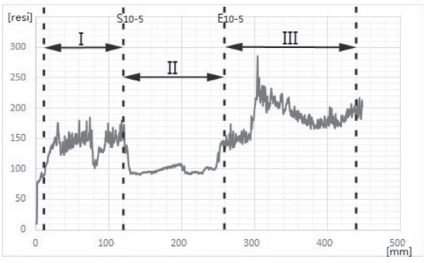

(e) Path 10-5

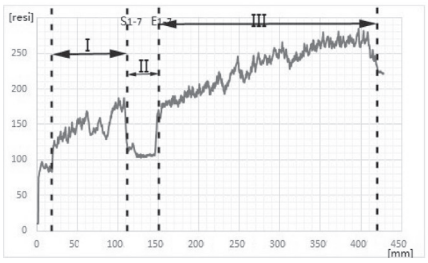

(f) Path 1-7

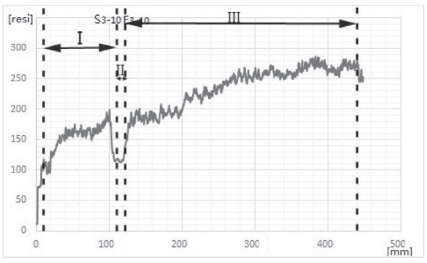

(g) Path 3-10

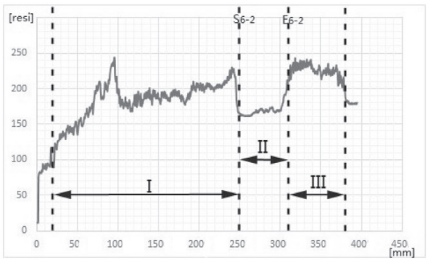

(h) Path 6-2

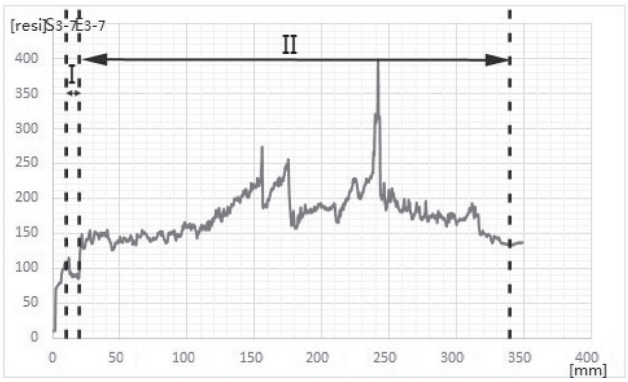

(i) Path 3-7

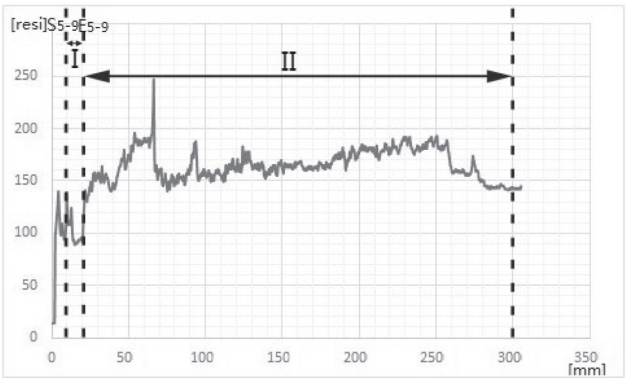

(j) Path 5-9

Fig. 8. Resistance curves of sample trees.

In Table 3, d_1 shows the length from $S_{i\text{-}j}$ to the i^{th} sensor and d_2 shows the length from $E_{i\text{-}j}$ to the j^{th} sensor in both resistance curves and tomographic images of SIRT and HWPM.

In sabina tree 2, SIRT failed to detect the decay along 6–12 drilling paths, so the comparison between SIRT and HWPM was not finished. Similarly, SIRT failed to detect the decay on the path 1–7 in cinnamon tree and the comparison was not finished too. When the comparison was made between d_1 or d_2 in resistance curves and tomographic

Table 3
The d comparison results of SIRT and HWPM.

Tree species	Path	d_1 (cm)	d_2 (cm)	SIRT		HWPM	
				d_1 (cm)	d_2 (cm)	d_1 (cm)	d_2 (cm)
Sabina 1	1–7	0	5	6	8	5	4
	4–10	8	7	12	14	6	9
Sabina 2	6–12	20	21	None	None	19.5	22.5
	7–12	14.5	6	10	16	10	14.5
	10–5	11	18	7	22	8	19
Cinnamon	1–7	9	27	None	None	7.5	28
	3–10	10	32	11	29	11	31
	6–2	23	7	28.5	1.5	25	8
Willow	3–7	0	32	0	32.5	0	32
	5–9	0	28	0	26	0	26

Table 4
The Δl comparison results of SIRT and HWPM.

Tree species	Path	l_0 (cm)	SIRT		HWPM	
			l_1 (cm)	Δl (%)	l_2 (cm)	Δl (%)
Sabina 1	1–7	35	26	25.7	31	11.4
	4–10	26	15	42.3	26	0.0
Sabina 2	6–12	2	0	100.0	1	50.0
	7–12	14	7.5	46.4	9	35.7
	10–5	14	10	28.6	16	14.3
Cinnamon	1–7	4	0	100.0	4.5	12.5
	3–10	1	3	200.0	1	0.0
	6–2	6	6	0.0	3	50.0
Willow	3–7	1	0.5	50.0	1	0.0
	5–9	1	3	200.0	3	200.0

images of SIRT and HWPM, the closer the value is, the more accurate the imaging method is. From Table 3, HWPM performs better than SIRT for evaluating the location of defective areas generally.

Furthermore, we used l to denote the defective length of drilling path, which can also reflect the size of the defective area on the whole cross-section. In Table 4, l_0 shows ground truth of l measured by Resistograph instrument, which can represent the defective degree of live trees. Similarly, l_1 and l_2 were the l values computed from the tomographic images of SIRT and HWPM. Δl denotes the relative error between l_1 or l_2 and l_0, which is defined by the Eq. (7). Here, l_c represents l_1 or l_2. The smaller Δl is, the more precise the imaging method is.

$$\Delta l = \left| \frac{l_0 - l_c}{l_0} \right| \times 100\% \tag{7}$$

In cinnamon tree, Δl of SIRT is smaller than Δl of HWPM along path 6–2, and this is because SIRT has detected the location of decay incorrectly of this path which can take the corresponding d value in Table 3 as a reference. Both methods have some false positive results for willow tree along path 5–9. The quantitative comparison results in Table 4 show that, HWPM performs better than SIRT for evaluating the size of defective areas, and accords well with the resistance curve in field testing experiments as a whole.

For the live trees, when processing the complicated defects, HWPM adopted both straight-ray and curved-ray propagation model for velocity inversion, and the location and the size of the defective areas were detected more precisely than SIRT. Tomograms of HWPM can locate moderate to severe internal decay in trees which accords well with the actual condition of trees, while tomograms of SIRT can only detect the slightly decayed area. In the process of the wave velocity inversion, HWPM imposed the maximum and the minimum velocity constraints on the grid cells. To improve the accuracy of tomographic images, cell-based constraints may be explored in the future to be applied into the velocity inversion. Each grid cell in the cross section can be assigned a parameter to constrain the velocity value. Besides, it's necessary to establish a more suitable initial velocity distribution for velocity inversion rather to assign the identical velocity value to each grid cell, and this needs enough understanding and experiences of wave velocity pattern in the live trees in the future work (Gao et al., 2012).

6. Conclusions

This paper presented a tomographic imaging method (HWPM) for nondestructive evaluation of the urban trees. By establishing the initial velocity distribution in advance, followed by the straight-ray and curved-ray inversion iterations with some velocity constraints imposed on the grid cells, HWPM can generate accurate tomographic images of the cross sections of live trees. The experimental results of several samples showed that HWPM had higher accuracy than SIRT in terms of the location, shape and size of the defective area. In the future, some other constraints may be explored into velocity inversion and the accuracy of tomographic imaging may be improved.

Acknowledgments

This study was supported in part by the National Natural Science Foundation of China (Grant No. 61472368), Key Research and Development Project of Jiangsu Province (Grant No. BE2016627), Wuxi International Science and Technology Research and Development Cooperative Project (CZE02H1706) and the Fundamental Research Funds for the Central Universities (Grant No. RP51635B).

References

Allison, R.B., Wang, X., Ross, R.J., 2006. Visual and Nondestructive Evaluation of Red Pines Supporting a Ropes Course in the USFS Nesbit Lake Camp. Sidnaw, Michigan.
Brancheriau, L., Ghodrati, A., Gallet, P., Thaunay, P., Lasaygues, P., 2012. Application of ultrasonic tomography to characterize the mechanical state of standing trees (Picea abies). J. Phys. Conf. Ser. 353, 1–13. http://dx.doi.org/10.1088/1742-6596/353/1/012007.
Divos, F., Divos, P., 2005. Resolution of stress wave based acoustic tomography. In: 14th Int. Symp. Nondestruct. Test. Wood, vol. 11, pp. 1–7.
Du, X., Li, S., Li, G., Feng, H., Chen, S., 2015. Stress wave tomography of wood internal defects using ellipse-based spatial interpolation and velocity compensation. BioResources 10, 3948–3962. http://dx.doi.org/10.15376/biores.10.3.3948-3962.
Espinosa, L., Cortes, Y., Prieto, F., 2017. Automatic segmentation of acoustic tomography images for the measurement of wood decay. Wood Sci. Technol. 69–84. http://dx.doi.org/10.1007/s00226-016-0878-1.
Feng, H., Li, G., Fu, S., Wang, X., 2014. Tomographic image reconstruction using an interpolation method for tree decay detection. BioResources 9, 3248–3263.
Gregory, S.G., Javier, O.B., Cesar, A.B., et al., 2016. Use of sonic tomography to detect and quantify wood decay in living trees 1. Plant Sci. Appl 1, 4. http://dx.doi.org/10.3732/apps.1600060.
Gao, S., Wang, X., Wang, L., Allison, R., 2012. Effect of temperature on acoustic evaluation of standing trees and logs: part 2 –field investigation. Wood Fiber Sci. 45 (1), 15–25.
Gao, S., Wang, N., Wang, L., Han, J., 2014. Application of an ultrasonic wave propagation field in the quantitative identification of cavity defect of log disc. Comput. Electron. Agric. 108, 123–129. http://dx.doi.org/10.1016/j.compag.2014.07.015.
Saito, H., 1989. Travel times and Ray paths of First Arrival Seismic Waves: Computation Method Based on Huygens' Principle. SEG, pp. 244–247.
Jackson, D.D., 1979. The use of a priori data to resolve nonuniqueness in linear inversion. Geophys. J. R. Astron. Soc. 57, 137–157. http://dx.doi.org/10.1111/j.1365-246X.1979.tb03777.x.
Jackson, M.J., Tweeton, D.R., 1994. MIGRATOM - Geophysical Tomography Using Wavefront Migration and Fuzzy Constraints. Book 38.
Kana, Y., Toshihiro, Y., Yuko, O., Hiroshi, Y., Izumi, Tokue, 2015. Detecting defects in standing trees by an acoustic wave tomography with pseudorandom binary sequence code: simulation of defects using artificial cavity. In: Ross, R.J., et al. (Eds.) Proceedings of the 19th International Nondestructive Testing and Evaluation of Wood Symposium. 22–25 September 2015, Madison, pp. 542–546.
Li, G., Wang, X., Feng, H., Wiedenbeck, J., Ross, R.J., 2014. Analysis of wave velocity patterns in black cherry trees and its effect on internal decay detection. Comput. Electron. Agric. 104, 32–39. http://dx.doi.org/10.1016/j.compag.2014.03.008.
Lin, C.J., Chung, C.H., Wu, M.L., Cho, C.L., 2013. Detection of Phellinus noxius decay in Sterculia foetida tree. J. Trop. For. Sci. 25, 487–496.
Merlo, E., Alvarez-Gonzalez, J.G., Santaclara, O., Riesco, G., 2014. Modelling modulus of elasticity of Pinus pinaster Ait. in northwestern Spain with standing tree acoustic measurements, tree, stand and site variables. For. Syst. 23, 153–166. http://dx.doi.

org/10.5424/fs/2014231-04706.
Socco, L.V., Sambuelli, L., Martinis, R., Comino, E., Nicolotti, G., 2004. Feasibility of ultrasonic tomography for nondestructive testing of decay on living trees. Res. Nondestruct. Eval. 15, 31–54. http://dx.doi.org/10.1080/09349840490432678.
Tweeton, D.R., 1992. BOMCRATR-A Curved Ray Tomographic Computer Program for Geophysical Applications. Minneapolis Mn U.S. Department of the Interior Bureau of Mines RI.
Wang, X., 2013. Acoustic measurements on trees and logs: a review and analysis. Wood Sci. Technol. 47, 965–975. http://dx.doi.org/10.1007/s00226-013-0552-9.